Lab on a Chip

PAPER

View Article Online
View Journal

Cite this: DOI: 10.1039/c9lc00612e

Deep, sub-wavelength acoustic patterning of complex and non-periodic shapes on soft membranes supported by air cavities†

Kuan-Wen Tung,[a] Pei-Shan Chung,[b] Cong Wu,[g] Tianxing Man,[a] Sidhant Tiwari,[c] Ben Wu,[bdef] Yuan-Fang Chou,[h] Fu-ling Yang[h] and Pei-Yu Chiou*[ab]

Received 26th June 2019,
Accepted 13th September 2019

DOI: 10.1039/c9lc00612e

rsc.li/loc

Arbitrary patterning of micro-objects in liquid is crucial to many biomedical applications. Among conventional methodologies, acoustic approaches provide superior biocompatibility but are intrinsically limited to producing periodic patterns at low resolution due to the nature of standing waves and the coupling between fluid and structure vibrations. This work demonstrates a near-field acoustic platform capable of synthesizing high resolution, complex and non-periodic energy potential wells. A thin and viscoelastic membrane is utilized to modulate the acoustic wavefront on a deep, sub-wavelength scale by suppressing the structural vibration selectively on the platform. Using 3 MHz excitation ($\lambda \sim 500$ μm in water), we have experimentally validated such a concept by realizing patterning of microparticles and cells with a line resolution of 50 μm (one tenth of the wavelength). Furthermore, massively parallel patterning across a 3 × 3 mm^2 area has been achieved. This new acoustic wavefront modulation mechanism is powerful for manufacturing complex biologic products.

Introduction

Methods for manipulating biological objects over the scales from micrometers to centimeters are the foundation to many biomedical applications, including the study of cell–cell interaction,[1,2] single-cell analysis,[3,4] drug development,[5] point-of-care diagnostics,[6–8] and tissue engineering.[9,10] Conventional methodologies deployed using optical,[11–14] magnetic,[15] and electrokinetic[16–18] forces are versatile, but they pose various deficiencies. Optical force can provide precise three-dimensional (3D) control of the manipulated objects but suffers from low throughput. Magnetic force is widely applied but it requires extra labeling of magnetic particles that could interfere with cell functions and downstream analyses. Other approaches based on electrokinetics, such as dielectrophoresis and electroosmosis, are simple to implement but are challenged by buffer incompatibility and electrical interference that could damage the manipulated samples. 3D printing[19,20] provides another means to form complex patterning profiles but has not been able to achieve precision control of its printed objects, thus limiting the resolution. Acoustic force, on the other hand, offers a potential avenue for noninvasive, label-free, and biocompatible manipulation.

Acoustic manipulation has attracted a lot of interest in the past for its superior biocompatibility and for its strength to control objects of sizes spanning from submicrometers to a few millimeters. Particles of different density and compressibility from the surrounding medium experience net acoustic radiation forces (ARF), incurred from a non-uniform acoustic field distribution, that transport them to either low or high potential energy regions. For a particle of size much smaller than the wavelength ($D \ll \lambda$), the ARF can be approximated by the following expressions:[21]

$$F^{\mathrm{rad}} = -\nabla U^{\mathrm{rad}} \quad (1a)$$

[a] Department of Mechanical and Aerospace Engineering, University of California at Los Angeles, 420 Westwood Plaza, Los Angeles, CA 90095, USA. E-mail: pychiou@g.ucla.edu; Tel: +1 (310) 825 8620
[b] Department of Bioengineering, University of California at Los Angeles, 410 Westwood Plaza, Los Angeles, CA 90095, USA
[c] Department of Electrical and Computer Engineering, University of California at Los Angeles, 420 Westwood Plaza, Los Angeles, CA 90095, USA
[d] Department of Materials Science and Engineering, University of California at Los Angeles, 410 Westwood Plaza, Los Angeles, CA 90095, USA
[e] Division of Advanced Prosthodontics, School of Dentistry, University of California at Los Angeles, 714 Tiverton Ave, Los Angeles, CA 90024, USA
[f] Department of Orthopedic Surgery, School of Medicine, University of California at Los Angeles, 10833 Le Conte Ave, Los Angeles, CA 90095, USA
[g] Department of Mechanical and Biomedical Engineering, City University of Hong Kong, Tat Chee Ave, Kowloon Tong, Hong Kong
[h] Department of Mechanical and Aerospace Engineering, National Taiwan University, No. 1, Section 4, Roosevelt Rd, Da'an District, Taipei City, 10617, Taiwan

† Electronic supplementary information (ESI) available. See DOI: 10.1039/c9lc00612e

$$U^{\mathrm{rad}} = \frac{4\pi}{3}a^3\left[f_1\frac{1}{2}\kappa_o\langle p^2\rangle - f_2\frac{3}{4}\rho_o\langle v^2\rangle\right] \quad (1b)$$

$$f_1 = 1 - \frac{\kappa_p}{\kappa_0} \quad (1c)$$

$$f_2 = \frac{2\left(\frac{\rho_p}{\rho_o} - 1\right)}{2\frac{\rho_p}{\rho_o} + 1} \quad (1d)$$

where F^{rad} is the ARF, U^{rad} is the acoustic potential energy, a is the radius of the particle, and p and v are the first-order acoustic pressure and velocity at the particle. The material compressibility κ and density ρ are subscripted by 'p' and 'o' for the particle and the surrounding medium, respectively. Two frequently used conventional acoustic mechanisms, bulk acoustic waves (BAWs)[22–25] and surface acoustic waves (SAWs),[26–39] have been applied to generate the non-uniform acoustic field. In BAWs, acoustically hard structures, such as silicon or glass microfluidic chambers, are fabricated to form resonant cavities. Acoustic frequencies matching with certain acoustic modes of the cavities are chosen to excite standing waves in these structures that form the non-uniform field. However, such a mechanism limits the particle patterning profile to be simple and periodic with a spatial resolution less than half of the wavelength ($1/2\lambda$). Although one can improve the resolution by increasing the acoustic frequencies, significant heating due to high energy attenuation can cause severe issues during manipulation of biological objects. In SAWs, standing and travelling waves are generated by an interdigitated transducer (IDT) typically fabricated on a piezoelectric substrate, such as lithium niobate ($LiNbO_3$). Due to its limited piezoelectric coupling and limited SAW-generation orientation however, $LiNbO_3$ prevents the creation of a complex field distribution whose formation requires wave components of different frequencies and orientations. Although dynamic patterning can be achieved by tuning the phases and frequencies of the electrical signals applied to the IDTs, the patterning profiles are often limited to periodic shapes. On the other hand, holographic acoustic tweezers using an acoustic hologram or an array of sound emitters can create patterns of complex shapes, but the spatial resolution is low.[40,41]

To date, there is no reported acoustic approach able to produce high resolution, complex and non-periodic potential energy wells. Here, we present a new type of acoustic wave modulation mechanism named Compliant Membrane Acoustic Patterning (CMAP) to overcome the aforementioned shortcomings for microobject and cell patterning.

Results

Operation principle of CMAP

CMAP is a device platform that allows the creation of deep, sub-wavelength resolution and complex, non-periodic acoustic potential wells near an engineered membrane. Such a potential landscape is realized by exciting acoustic traveling waves, generated using a piezoelectric ceramic PZT (lead zirconate titanate), to pass through desired shapes of air cavities sized much smaller than the wavelength and embedded in a soft, viscoelastic polydimethylsiloxane (PDMS) structure, as illustrated in Fig. 1. PDMS is chosen since its acoustic impedance is close to that of the surrounding fluid (water) for which the wave reflection at the PDMS/water interface can be minimized.[42] Air cavities are utilized since they have a large acoustic impedance difference to most materials for which

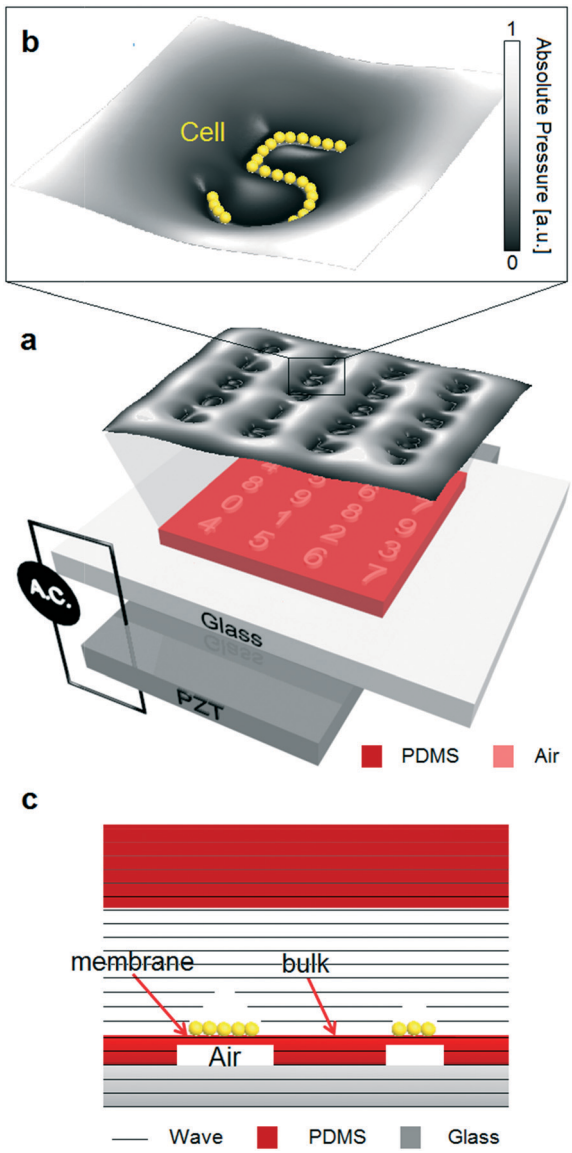

Fig. 1 CMAP device platform that enables arbitrarily shaped, deep subwavelength particle patterning. (a) The device assembly consists of a PZT substrate as the power source, a glass intermediate allowing reattachment of the above air-embedded PDMS structure, and the PDMS structure that selectively blocks incoming acoustic travelling waves using air cavities. (b) A representative schematic of the resulting acoustic radiation potential field distribution immediately above the PDMS structure is shown. (c) Cross-sectional view of the assembly shows the bulk and membrane regions of the PDMS structure, as well as a PDMS encapsulation that is designed to attenuate wave propagation and prevent wave reflection back into the chamber.

the majority of the waves can be reflected.[43,44] As a result, near-field acoustic potential wells are formed immediately above the air cavities with a spatial resolution matching to the cavities' size. A thick PDMS layer atop the water layer serves as a wave-absorbing medium to prevent acoustic waves from reflecting back (see the Experimental section for details on device design and assembly).

One major challenge encountered in conventional acoustic patterning is the coupled fluid and structure vibration that complicates the design of the device structure. With the CMAP platform, we are able to minimize the effect of structure-induced vibration that would otherwise interfere with the intended acoustic field and, ultimately, able to predict the shape of particle patterning by using a simple pressure wave propagation model. This innovation can be carried out by incorporating a thin and compliant, viscoelastic PDMS membrane to interface the air cavities and the above chamber fluid. When the pressure waves propagate through the air-embedded PDMS structure, the vibration in the bulk decays within a short distance into the membrane due to two primary characteristics. One characteristic is the membrane's thinness and compliance for which it does not have sufficient stiffness to drive and move the fluid mass atop at high frequency. The second characteristic stems from material damping of the structure at high frequency that prevents the vibration energy from building up in the membrane region. Thus, the fluid pressure above the membrane region does not fluctuate much with the waves that propagate through the bulk into the fluid and remains at a relatively constant level compared to regions in the bulk. This creates a low acoustic pressure zone above the membrane and establishes a pressure gradient between the bulk and membrane regions. Since this near-field pressure zone depends on the membrane area attained from the air cavities that can be fabricated into any size and geometry, complex and non-periodic particle patterning with a spatial resolution much smaller than the wavelength can be realized. Additionally, large area patterning can be achieved using the same actuation principle; for the fact that the PZT substrate generates plane acoustic waves with uniform intensity, the maximum operating area is only limited by the PZT's available size. In short, since the acoustic potential landscape of CMAP does not rely on the formation of standing waves and since the disturbance of the landscape due to the structure-induced vibration may be minimized, the shape of potential wells simply reflects that of the air cavities.

To quantitatively understand the operation principle of CMAP, we study the relationship between the material properties of PDMS and their effects on structure-induced vibration using numerical simulation. A COMSOL acoustic–structure interaction model is implemented, as shown in Fig. 2 (see the Experimental section for simulation details on the model). The model geometry considers a 50 μm wide air cavity embedded in a PDMS structure that leaves a 2 μm suspended membrane interfacing an above incompressible fluid (water). The relationship $\eta_s = E''/E'$, where E' is the dynamic storage modulus, E'' is the dynamic loss modulus, and η_s is the isotropic loss factor of the PDMS structure accounting for the structural damping, is explored under a sinusoidal excitation frequency of 3 MHz. For simplicity, η_s is assumed to be constant (0.2) while the moduli are varied. Fig. 2a examines the vertical displacement of the PDMS surface interfacing the fluid. Strong membrane vibration is observed for the structure of high E' at 100 MPa. This opposes the case of low E' at 0.1 MPa in which the structure-induced vibration from the bulk decays substantially in a short distance at the membrane edge, leaving the membrane relatively flat and smooth. The softness and lightness of the membrane enable it to follow the motion of water when cycling through different phases of the excitation (Fig. 2b). Under ideal operation conditions, as acoustic waves travel through the patterned PDMS structure, the surface oscillation motions of the membrane and the bulk should be in the opposite direction, or out of phase. When the water above the bulk is being displaced upwards at phase 90 deg., the developed pressure drives the water downward, deforming the membrane to satisfy mass conservation ($\nabla \cdot V = 0$) since it occurs on a length scale much shorter than the acoustic wavelength ($d \ll \lambda$). When the water above the bulk moves downwards at phase 270 deg., the water atop the membrane flows back to the bulk region. These back-and-forth fluid motions are repeated under sinusoidal excitation.

The acoustic radiation potential landscape is estimated by accounting the resulting water pressure and velocity fields near the PDMS–fluid interface into eqn (1b). For 10 μm polystyrene beads (ρ_p = 1050 kg m^{-3}, κ_p = 2.38 × 10^{-10} Pa^{-1}),[45,46] the potential profile at 5 μm above the air-embedded PDMS structure of E' at 100 MPa, Fig. 2c, reveals strong variation that leads to multiple metastable wells across both the membrane and bulk. On the other hand, the potential profile for the structure of E' at 0.1 MPa shows a much smoother landscape with wells generated only in the membrane region, resulting in a bead patterning shape that conforms to that of the air cavity. Minimum potential wells occurred at the membrane edges rather than at the center because the perturbed pressure term in eqn (1b) is weak and the velocity term dominates in these regions. The relative contributions of the pressure and velocity terms in the potential profile can be better explained by the energy density plots, $\frac{1}{2}\kappa_o\langle p^2\rangle$ and $-\frac{3}{4}\rho_o\langle v^2\rangle$, in Fig. S1† and their multiplication with the particle property factors (f_1 = 0.465 and f_2 = 0.032 for polystyrene beads in water). The large f_1 factor, compared to f_2, allows the pressure term to dominate in most regions except at the membrane. The fluctuation of the potential profiles in the membrane region in Fig. 2c is primarily attributed to the velocity term. Nevertheless, from the potential profile simulated for the case of the structure of E' at 0.1 MPa, it can be predicted that the beads will begin accumulating at the membrane edges then eventually move toward the center as more beads fill in from the bulk.

In contrast, for PDMS beads (ρ_p = 965 kg m^{-3}, κ_p = 8.95 × 10^{-10} Pa^{-1}, f_1 = −1.011, f_2 = −0.024) that exhibit greater

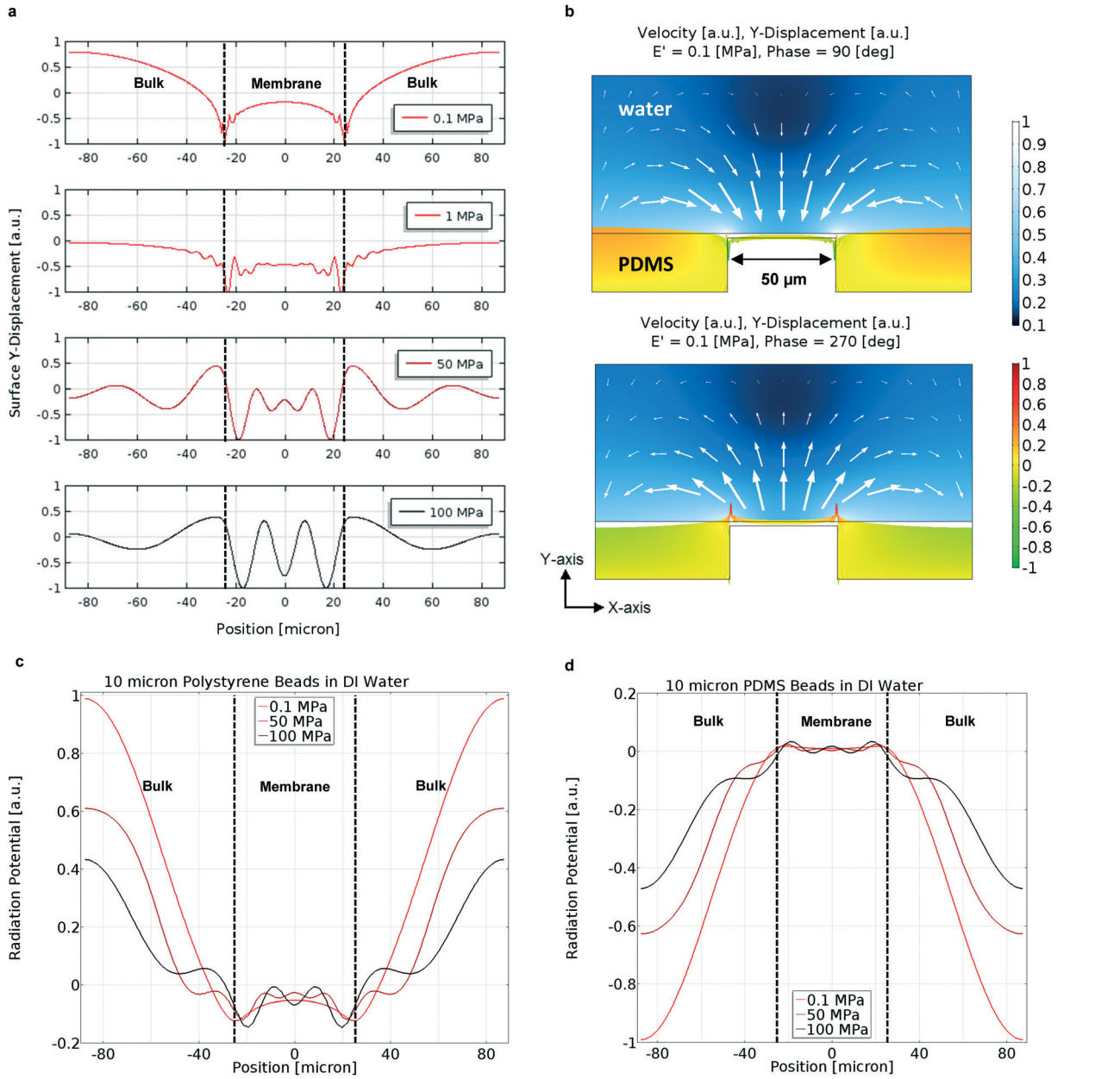

Fig. 2 Acoustic–structure interaction simulations investigating the effect of changing the material properties of PDMS. During vibration, the surface of an air-embedded PDMS structure interfacing the chamber fluid shows a smoother profile (a) and lower order structure vibration mode when the E' of the structure decreases from 100 MPa to 0.1 MPa. This is especially noticeable in the membrane region. (b) Such a change in E' gives rise to the compliance of the membrane to the above fluid such that upward displacement of fluid above the bulk drives the fluid downward, deforming the membrane, *vice versa*. The resulting acoustic potential landscapes, 5 μm above the PDMS structure, for 10 μm polystyrene beads (c) and 10 μm PDMS beads (d) in water are simulated. For the polystyrene beads, a high E' creates multiple potential wells across both the bulk and membrane regions while a low E' creates potential wells conforming to the membrane area; notice that all the minimum potential wells are generated at the membrane edges. In contrast, PDMS beads with higher compressibility revert the potential profiles.

compressibility than water, the compressibility reverts the profiles in Fig. 2c which leads to trapping of the beads in high-pressure regions outside the air cavity as illustrated in the simulated results in Fig. 2d. In addition, it has been shown that the speed of sound of PDMS can drop rapidly from ~1000 m s^{-1} to ~40 m s^{-1} when the porosity varies from 0 to 30%.[47] Based on the relationship $\kappa_p = 1/\rho c^2$, where c is the speed of sound, the high compressibility of porous PDMS can result in an f_1 factor orders of magnitude larger than f_2, allowing the pressure term to further dominate.

As simulated, the compliant, viscoelastic PDMS membrane effectively limits the structure-induced vibration propagating from the bulk into the membrane region. This unique feature permits membranes of sizes larger than the propagation length to be utilized for complex and non-periodic patterning on CMAP. In Fig. S2,† the vibration from the bulk decays in

~10 μm from the edges of the PDMS membrane (E' at 0.1 MPa), regardless of the membrane width. In other words, the design process to create a desired potential landscape is greatly simplified *via* bypassing the complicated analysis of fluid–structure interaction and acoustic modes encountered in conventional acoustic devices.

To evaluate the simulated results, we fabricated the CMAP platform using two types of PDMS of different Young's moduli, E, to form the air-embedded, viscoelastic structures and then performed laser Doppler vibrometer (LDV) measurements over their surfaces. The first type was synthesized following the manufacturer's instructions using Sylgard 184 (Dow Corning Co.) to produce an E of ~1750 kPa, and the second type was synthesized as a mixture of Sylgard 527 (Dow Corning Co.) and 184 at a weight ratio of 4 : 1 to produce an E of ~250 kPa.[48] Although these are static moduli, a decrease in E is accompanied by a decrease in both the dynamic moduli, E' and E''.[49] Hence, the two compositions

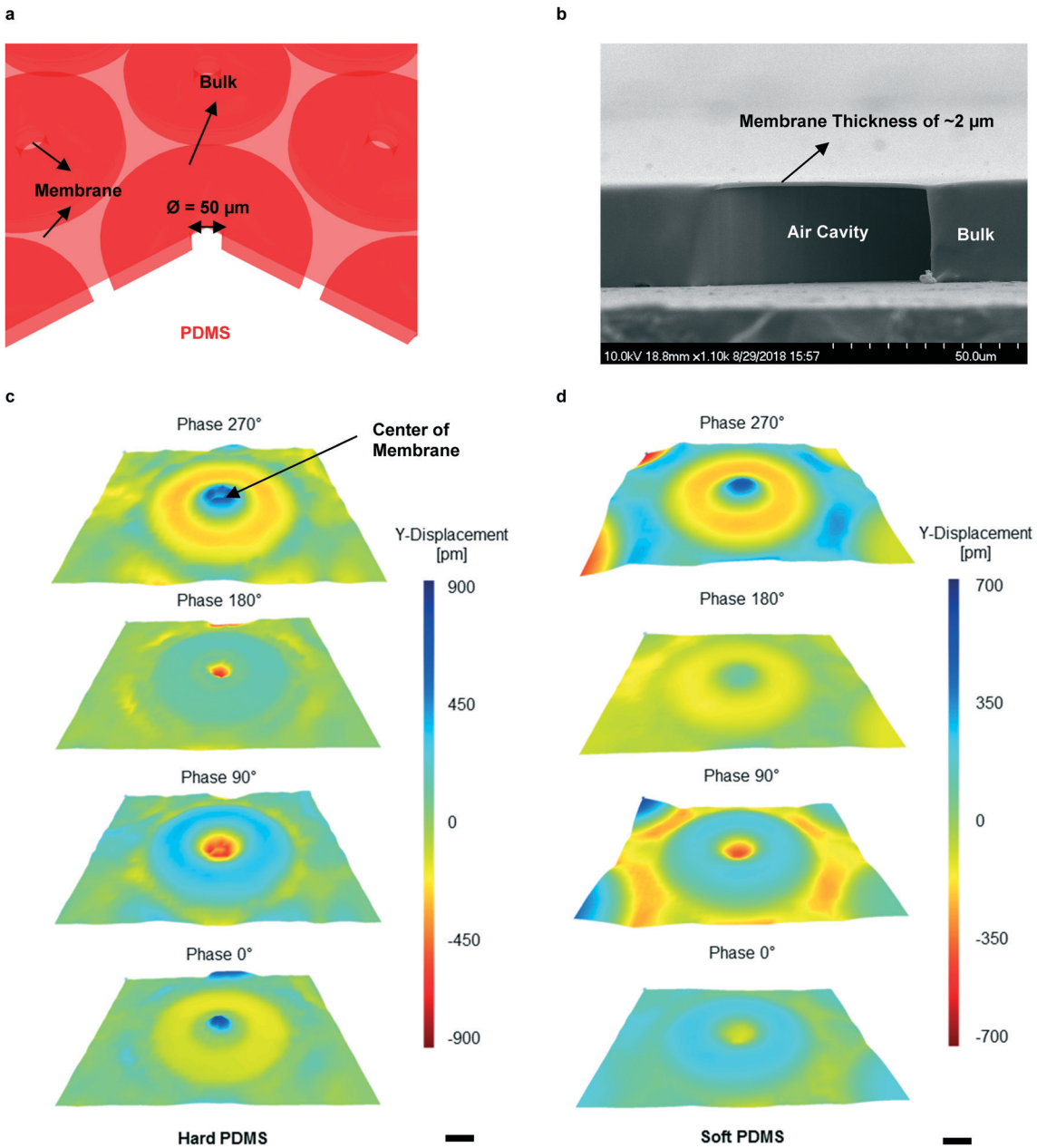

Fig. 3 Laser Doppler velocimetry (LDV) measurements of the vertical surface displacement of hard and soft, air-embedded PDMS structures cycling through different phases of sinusoidal excitation at 3 MHz. The hard and soft PDMS of high and low E', respectively, exhibiting varying surface vibration patterns are demonstrated using a concentric ring-structure (a). The SEM cross-section of a fabricated sample (b) is shown (see the Experimental section for thickness measurement of the PDMS membrane). During the excitation, the surface profiles between the two PDMS structures (c and d) are noticeably different at the center membrane. Not only does the hard PDMS structure generate a higher order structure vibration mode but it also creates a larger area of membrane vibration relative to the bulk. Scale bar, 50 μm.

became the hard and soft, air-embedded PDMS structures representing the simulated cases of E' at 100 MPa and 0.1 MPa, respectively. A schematic diagram representing the PDMS structures (an array of concentric rings), Fig. 3a, is shown together with a SEM (scanning electron microscopy) cross section, Fig. 3b, of a fabricated sample. Driven under similar operation conditions to those set in the simulations, the surface vertical displacements of the hard and soft PDMS structures, Fig. 3c and d, respectively, are measured over a cycle of acoustic excitation. Movies S1 and S2† also demonstrate the structures' LDV measurements over the cycle. For the hard PDMS structure, the surface profiles at phase 90 and 270 deg. show structural perturbation that propagates deeply into the center of the membrane which excites the high-order structure vibration mode, resembling the simulation results for E' at 50–100 MPa, Fig. 2a. For the soft PDMS structure at the same phases however, the displacement profiles at the center of the membrane are smooth and resemble those of simulated E' in the range between 0.1 and 1 MPa, Fig. 2a. Of note here is that, in addition to the difference between the dynamic and static moduli, variation in PDMS thickness could modify its mechanical properties.[50]

Complex and non-periodic patterning of microparticles

Complex and non-periodic particle patterning has been a major complication in the field of acoustofluidics, where the patterning resolution and profile are restricted by attainable wavelength size and limited, periodic acoustic potential landscapes, respectively. Alternatively, the new acoustic patterning mechanism using the CMAP platform allows us to overcome these challenges. As illustrated in Fig. 4, 10 μm polystyrene beads in water are patterned using the prior hard and soft, air-embedded PDMS concentric ring-structures at an operating frequency of 3 MHz and voltage of 5 V_{rms}. While both structures demonstrate patterns that conform to the shape of membranes/air cavities, the hard PDMS structure in Fig. 4a exhibits an additional trapping profile in the bulk region. This is exemplified by the simulation, Fig. 2c, that the PDMS structure of high E' at 100 MPa creates extra metastable potential wells in the bulk region. Both the experimental and simulation results show additional wells generated ~20 μm away from the membrane edges. In contrast, the soft PDMS structures in Fig. 4b–d show trapping profiles only at the membrane edges. For the simulated PDMS structure of low E' at 0.1 MPa, Fig. 2c, effective damping of wave propagation into the membrane provides membrane compliance to the above fluid motion where, and only where, the potential wells are generated. At low concentration of beads, Fig. 4b and Movie S3,† trapping began at the membrane edges, where the lowest acoustic potentials reside as explained before. Such trapping was realized over a repeated concentric ring-pattern spanning over 3 × 3 mm^2. Furthermore, as observed from the lining of the beads between the neighboring rings, a spatial resolution of 50 μm has been achieved, which is 10 times lower than the applied acoustic wavelength (~500 μm). This

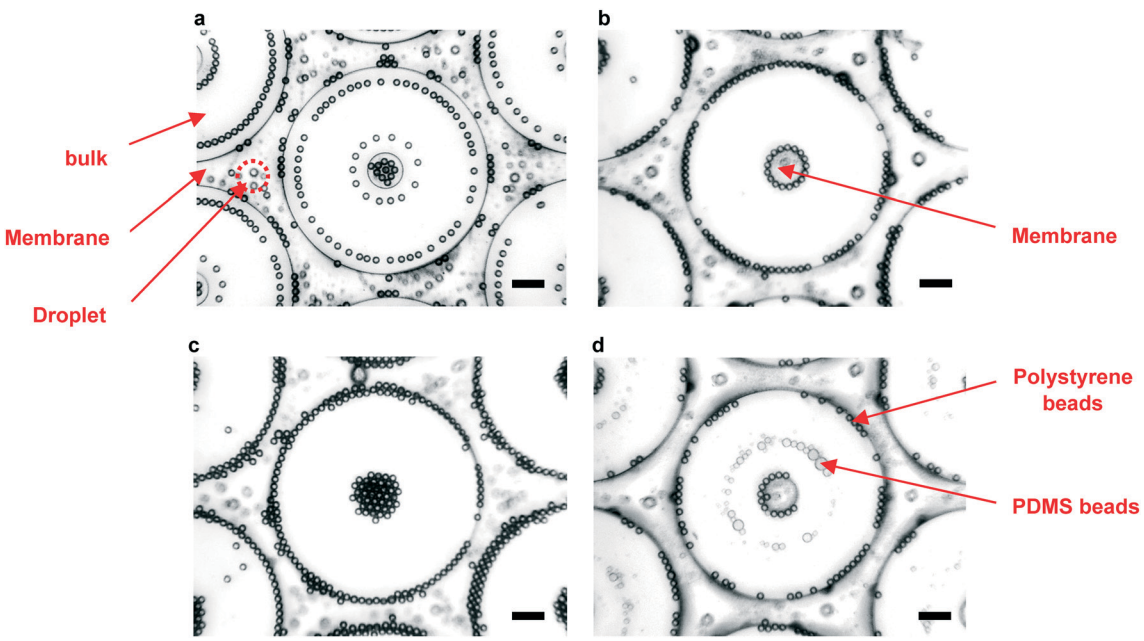

Fig. 4 Patterning of microparticles in water using hard and soft, air-embedded PDMS structures in the shape of concentric rings. Hard and soft PDMS compositions are used to fabricate the concentric ring structures for comparison. The hard PDMS structure (a) leads to multiple patterns of 10 μm polystyrene beads across the bulk and membrane regions. The soft PDMS structure (b and c) enables clean patterning profiles precisely following the shape of air cavities. At low concentration (b), the beads are aligned with the edges of membranes where the lowest potential wells reside. At high concentration (c), the beads initially trapped at the edges were pushed into the membrane region where there are more beads than what the edges can hold. In a mixture (d), polystyrene and PDMS beads migrate to the locations of low and high pressure, respectively, corresponding to the potential landscapes simulated in Fig. 2c and d. Notice that water droplets are formed beneath the suspended membranes. Scale bar, 50 μm.

indicates the subwavelength resolution capability of CMAP as compared to other conventional acoustic approaches; Fig. S3A–C and D–F† further demonstrate the capability using soft, air-embedded PDMS stripped and circular-structures, respectively, spaced at 20 μm, 50 μm, and 100 μm apart, and the results conform to the 50 μm spatial resolution achieved. At higher concentration, Fig. 4c, beads initially trapped on the edges of the membrane are pushed toward the center, thus filling up the entire membrane space. Patterning of the mixture of polystyrene and PDMS beads, Fig. 4d, is also demonstrated; the result conforms to the simulations that the PDMS beads would accumulate in the high-pressure region in contrast to the polystyrene beads. This contrast reflects CMAP's potential applications such as particle sorting and visualization of acoustic waves.[51–53] In the future, CMAP may be redesigned to include soft, air-embedded PDMS structures of channel shape for particle sorting. Overall, using the soft PDMS rather than the hard PDMS as the air-embedded structure leads to clean profiles of patterning.

To further assess CMAP's ability in complex and non-periodic pattering, we fabricated another set of soft, air-embedded PDMS structures consisting of numeric characters. At high concentration, Fig. 5a and Movie S4,† 10 μm polystyrene beads in water completely filled up the membrane regions, however, with additional traces that are especially noticeable in the characters "1", "6", and "8". This is due to the wave interferences between the neighboring air cavities when the size of the bulk region exceeds the acoustic wavelength. These traces, circled in red, are well captured by the acoustic pressure simulation, Fig. 5b, that considers only the pressure aspect among all the device phenomena observed; the effect of fluid structure interaction was not accounted. The dark blue color represents the lowest value of absolute pressure mirroring the region of lowest acoustic potential. Fig. 5c shows the 3-D model geometry used in the simulation; the geometry is constructed with true dimensions in accordance to the fabricated soft PDMS structures (see the Experimental section for the technique on acoustic pressure simulation). The close resemblance between the experimental and simulation results reflects the simplicity of using the CMAP mechanism to design a device that forms complex and non-periodic acoustic potential profiles.

Complex and non-periodic patterning of biological cells

Similar to polystyrene beads, patterning of cells highly depends on the surface displacement of the soft, air-embedded

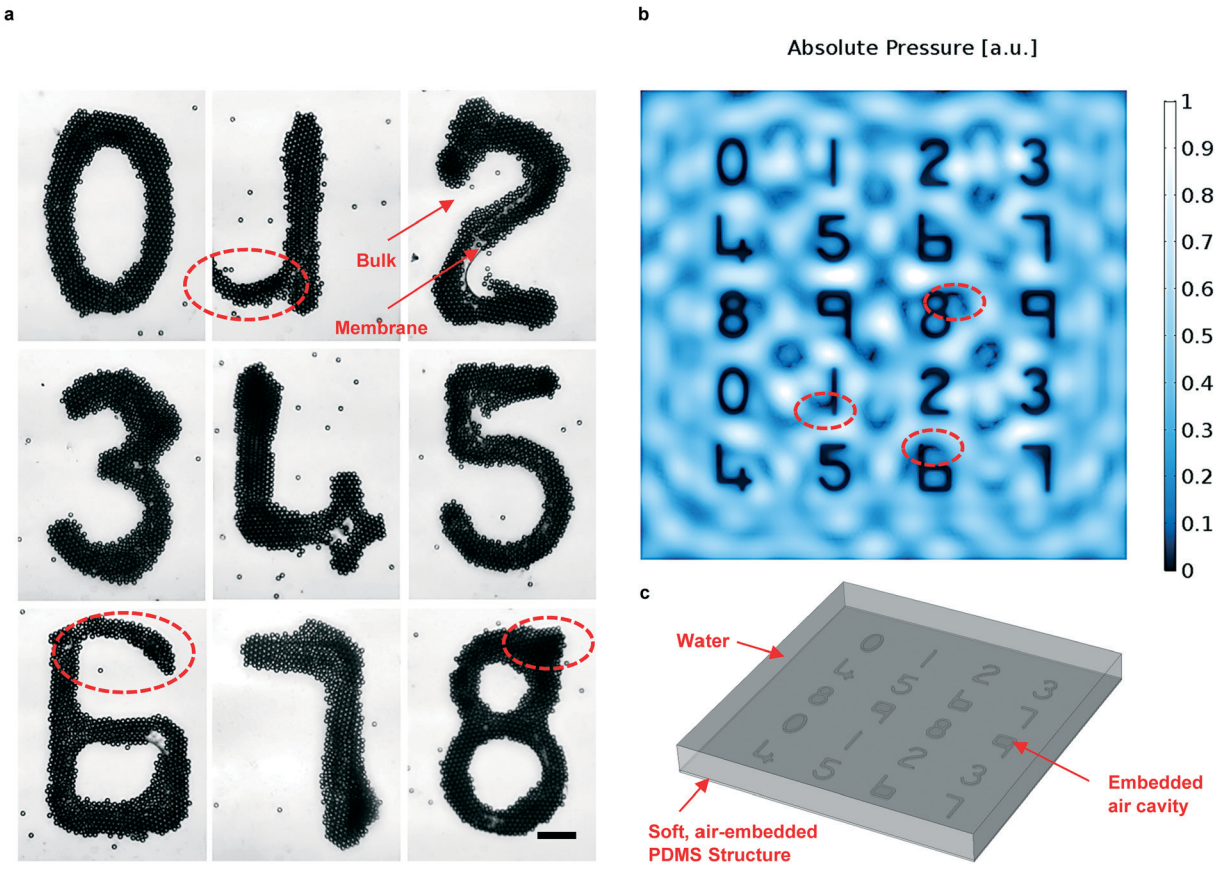

Fig. 5 Patterning of microparticles in water using soft, air-embedded PDMS structures in the shape of numeric characters, and their corresponding acoustic pressure simulation. Soft PDMS enables precise and arbitrary patterning of 10 μm polystyrene beads (a). Although there are additional traces, circled in red, in both the patterning profiles and the simulated pressure landscape (b) that is directly above the PDMS structure, the trappings conform closely to the simulation. The simulation is performed using the 3-D model geometry (c), which consists of top fluid and bottom PDMS with embedded air cavities, similar to the aforementioned acoustic–structure interaction model in Fig. 2. Scale bar, 70 μm.

PDMS structure, as well as the density and compressibility of the particles and their surroundings, which gives rise to the acoustic potential landscape. HeLa cells (see the Experimental section for details on cell culturing) are chosen here to verify the biocompatibility of the CMAP platform. Since typical cells (ρ_p = 1068 kg m^{-3}, κ_p = 3.77^{-10} Pa^{-1} as in the case of breast cells)[54] in DMEM have similar properties to polystyrene beads in water, their potential landscapes formed using the same soft PDMS structure should be nearly identical. As illustrated in Fig. 6a and Movie S5,† patterning of HeLa cells in the shape of numeric characters resembles that of the polystyrene beads in Fig. 5a.

Numerous acoustic approaches for cell patterning have been assessed in determining cell viability and proliferation, and prior approaches in MHz-order acoustic fields have proven to be biocompatible.[27,55–57] Our CMAP device platform, in a similar MHz-order of operation, provides comparable results. To prevent potential thermal damage due to heat accumulation on our platform, we operated the device with a T.E. cooler set at 12 °C to control the chamber temperature (see the Experimental section for the setup and operation). Fig. 6b illustrates the temperature as a function of time at an operating frequency of 3 MHz and voltage of 5 V_{rms}. The operation needs approximately 5 minutes before a steady state (~22 °C) is reached, a temperature less than the cell incubation at 37 °C. Furthermore, viability assessment using trypan blue (ATCC) and cell counts using a hemacytometer (Hausser Scientific Reichert Bright-Line), following the manufacturers' protocols, are performed on the HeLa cells operated in the device under the same experimental conditions for 5 minutes; the outcome shows a similar level of viability at 96.73% to that of the control at 94.52%, Fig. 6c. Assessment of cell proliferation also shows promising results. After the experiment, portions of the cells were incubated for 48 hours (from day 1 to day 3). Using a hemocytometer, we have approximated the densities of cells at day 1 and at day 3 for both the experiment and control which all indicate an increase of more than three-fold, Fig. 6d. The increase corresponds to the HeLa cell doubling time that is approximately 24 hours.[58]

Discussion

We have demonstrated the CMAP platform as a powerful tool to realize deep sub-wavelength, complex and non-periodic patterning of microparticles and biological objects. These are achieved using a suspended, thin and compliant PDMS

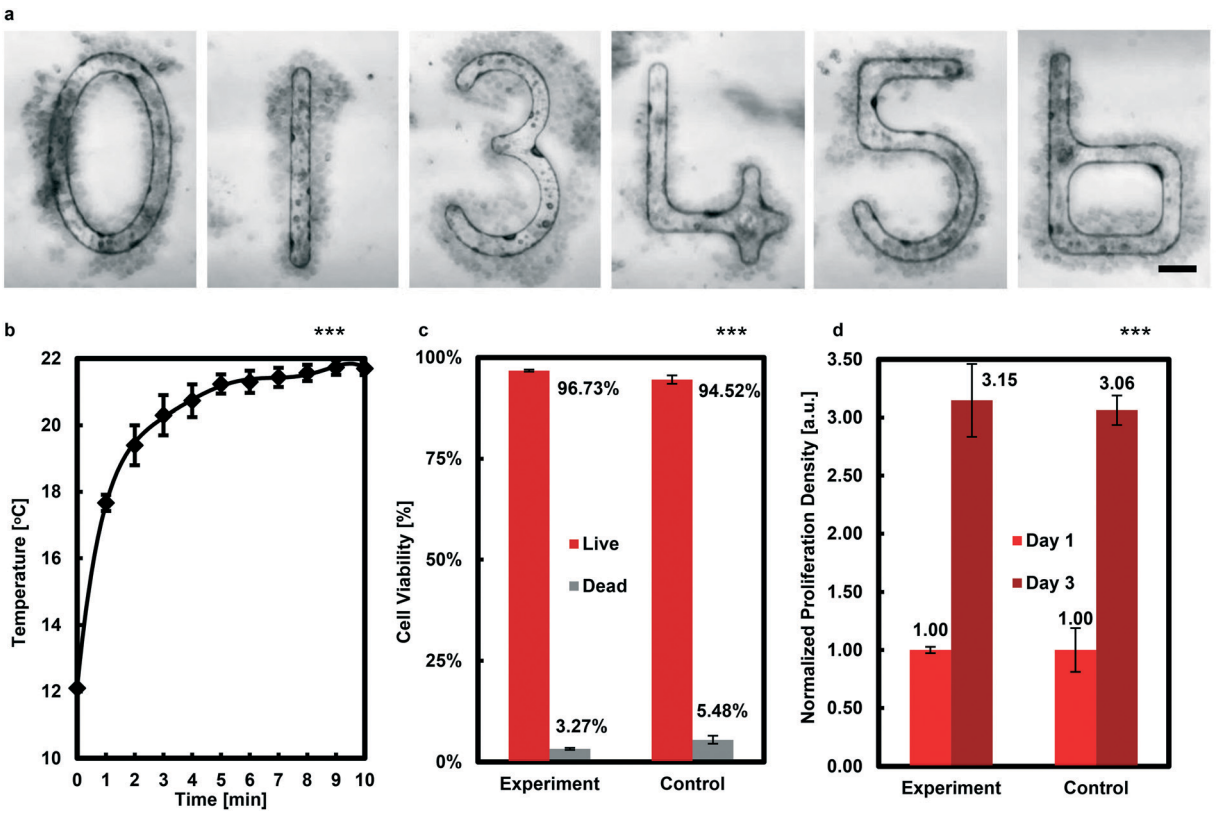

Fig. 6 Patterning and viability assessments of HeLa cells in DMEM using soft, air-embedded PDMS structures in the shape of numeric characters. (a) Similar to the polystyrene beads in Fig. 5a, HeLa cells can be patterned into arbitrary shapes using soft PDMS. Due to heat generation of PZT, however, the CMAP device platform is operated on a T.E. cooler to maintain the chamber temperature; the temperature as a function of time (b) is measured and the result shows a steady state at approximate 22 °C. (c) After 5 min of continuous operation in the device at the applied frequency of 3 MHz and voltage of 5 V_{rms}, cells show comparable viability (96.73%) to that of the control (94.52%). (d) Additionally, cells from both the control and experiment proliferated by more than three-fold over a period of two days (48 hours), demonstrating the biocompatibility of the CMAP platform. Scale bar, 70 μm (***number of trials measured, n = 3).

membrane that minimizes the effect of structure-induced vibration and that adapts to the surrounding fluid motion without offsetting the intended acoustic potential landscape. The membrane can be of any geometry, making complex and non-periodic patterning possible. Additionally, both the PZT and the soft, air-embedded PDMS structure can be scaled up for larger area patterning based on the underlying acoustic actuation principle.

Of note here is that since the ARF in eqn (1b) includes both the velocity and pressure terms which are usually coupled in practical applications, it is difficult to design a device optimized for acoustic patterning that utilizes both terms. For the CMAP platform, the device is designed for patterning based on the pressure term. Microparticles, such as polystyrene beads and most biological objects, that have a similar density but different compressibility from water ($f_1 \gg f_2$) are ideal objects to be patterned on the CMAP device. For particles with a large density difference from water such as gold beads ($f_1 \sim 0.99, f_2 \sim 0.90$), the velocity term can become significant. Nevertheless, the patterns formed by these particles should also conform to the shape of air cavities since the cavity edges are where the maximum velocity locates as shown in Fig. S1B.†

Although acoustic streaming force, ASF,[59] can be induced to counterbalance the ARF and disturb the patterning, our experimental results suggest that ARF is the driving force when the operation frequency is above 3 MHz and the particle is sized 10 μm or larger. At the onset of the operation, streaming vortices, as illustrated by the 1 μm polystyrene beads in Movie S3,† are observed only at the center of the circular membrane and extend weakly to ~25 μm near the edge. On the other hand, the 10 μm polystyrene beads that were spread across the device migrate toward the membrane edges, where they are trapped firmly despite the later bulk movement of the fluid as shown by the 1 μm beads. This strong trapping effect implies the dominant strength of ARF to the patterning of 10 μm beads. We also refer to the observed phenomenon of the bulk movement as global flow, induced by the volumetric change of the chamber as the upper PDMS lid expands thermally due to heat generation from PZT. Since the upper PDMS lid (~1 cm) is substantially thicker than the bottom soft, air-embedded PDMS structure (~27 μm), the volumetric change should be predominately caused by the expansion of the lid.

PDMS is a material with strong acoustic energy attenuation properties, a potential problem that needs to be properly addressed when designing acoustofluidics devices. In our CMAP device, the acoustic waves generated at the bottom substrate propagate through the thin, air-embedded PDMS structure, into the chamber fluid, and then into the PDMS lid. The thickness of the lid is designed to be 1 cm, which enables sufficient wave energy attenuation at our operating frequency of 3 MHz to prevent reflection from the interface between ambient air and the device. At 3 MHz, the attenuation coefficient of PDMS is 10.14 dB cm^{-1}, which allows the lid to absorb >99% of wave energy before reflecting back to the chamber fluid.[60,61] Note that the thickness of the air-embedded PDMS structure of 27 μm is much smaller than that of the lid, rendering the wave energy attenuation at the structure negligible.

Movies S4 and S5† show that the 10 μm polystyrene beads and HeLa cells, respectively, outside the air cavities drift away because these are in excess to what the potential wells above the cavities can hold. Note that such drifts are mainly caused by the global flow for the reason that the ASF is only effective near the membrane edges. The drifts are favorable to us because they lead to overall cleaner patterning profiles without excessive targets outside the cavities. Notice that the images in Movies S3–S5† get blurred toward the end. We suspect that the thermal expansion of PDMS has caused structural deformation which affected the microscope focusing. Besides the global flow, patterning of the 10 μm beads and HeLa cells reveals conformities to the pressure distribution simulated in Fig. 5b, further defying the significance of acoustic streaming.

We have chosen 3 MHz as the operation frequency because it is a high enough value to suppress the acoustic streaming flow and a low enough value to avoid extra acoustic heating. For example, when the operation frequency is lowered to 0.5 MHz, 10 μm polystyrene beads can follow the streamlines of 1 μm beads, circulating in vortex form near the membrane edges as demonstrated by Movie S6.† This leads to unstable patterning and difficulty in achieving the desired profile. On the other hand, while operation at higher frequency can minimize the streaming flow, it is accompanied by larger energy attenuation in PDMS and, thus, extra heat generation that needs to be managed.[60]

While the CMAP platform relies on a compliant, viscoelastic PDMS membrane to provide the breakthroughs in patterning, the membrane is so thin (~2 μm) that the above fluid can penetrate through. This is evident in the fluid droplets below the membrane regions as shown in Fig. 4. Prior studies,[62,63] too, have demonstrated that PDMS is porous in nature which enables water molecules to diffuse through it. Accounting for the additional acoustic vibrations during the device operation, the fluid could have penetrated through the thin membrane which generated the droplets. Accumulation of the droplets could also affect particle patterning; if sufficient droplets are accumulated (*e.g.* filling up the air cavities), the membrane would no longer be fluid compliant and the patterning profile would be distorted. In order to avoid such a problem, future work is needed to identify an approach, either through thin film coating or surface treatment, to prevent water penetration while maintaining the compliant characteristic of the membrane.

Experimental section

Device design and assembly

The CMAP device, Fig. 1, consists of a PZT substrate (lead zirconate titanate), soda-lime glass, and top and bottom PDMS structures. The PZT of dimensions 3 cm × 1 cm × 0.05

cm ($L \times W \times H$) from APC International Ltd. and of material type 841 generates acoustic travelling waves across the device. On the top, a soda-lime glass slide from Corning (Model 2947-75 × 50) dimensioned 2 cm × 2 cm × 0.1 cm ($L \times W \times H$) is affixed using epoxy. Glass allows easy reattachment of the soft, air-embedded PDMS structure which makes the PZT substrate reusable. The soft PDMS structure is fabricated, in a similar fashion to the standard PDMS replica molding,[64] using a mixture of Sylgard 527 and 184 in a weight-to-weight ratio of 4 to 1. The master mold is composed of MicroChem Corp's SU-83025 micro-structures photolithography-patterned on a silicon wafer which shapes the embedded air cavities. The molding process is carried out by covering the master mold in the Sylgard mixture and then stamping using another slide of glass topped with aluminum block (~7500 g). As a result, an ~2 μm thick meniscus is formed on the micro-structures and it becomes the PDMS membrane (see the SEM image in Fig. 3b). For the soft PDMS structure, curing of the mixture is performed at room temperature. For the hard PDMS structure also demonstrated in the experiments, the molding process differs by using pure Sylgard 184 cured in an oven at 70 °C for 4 hours. Subsequently, the soft/hard PDMS structure is transferred onto the device's glass layer. Microparticles or biological objects are then pipetted onto the structure and encapsulated with a thick PDMS. To minimize wave reflection inside the device's chamber, PDMS of Sylgard 184 is used as the encapsulation for its close acoustic impedance to that of water. In addition, the thickness of the encapsulation is designed to be 1 cm, which enables sufficient wave energy attenuation at our operating frequency of 3 MHz to prevent reflection from the interface between ambient air and the device.[60,61]

Setup and operation

The complete setup for using the CMAP device involves a power amplifier (ENI Model 2100L), a function generator (Agilent Model 33220A), a T.E. cooler (T.E. Technology Model CP-031HT), an ultra-long working distance microscope lens (20× Mitutoyo Plan Apo), an upright microscope (Zeiss Model Axioskop 2 FS), and a mounted recording camera (Zeiss Model AxioCam mRm). Surfaces of the PZT substrate are wire-bonded and electrically connected to the power amplifier that is controlled by the function generator to feed the A. C. signals. Upon receiving the signals, the PZT transforms the sinusoidal voltages into mechanical vibrations to generate the acoustic traveling waves across the device. To prevent cell damage from excessive PZT heating, we operated the device on a T.E. cooler set at 12 °C. To monitor the temperature of the device's chamber, we inserted a thermocouple (Omega OM-74) through the PDMS encapsulation and reran the experiment with only water in the chamber; the result shows stabilization below the incubation temperature of 37 °C, suggesting suitability for long-term operation. The entire assembly is positioned under the Mitutoyo microscope lens mounted on the Zeiss Axioskop. The patterning process is then observed through the PDMS encapsulation that allows clear visualization and is recorded using the accompanying Zeiss AxioCam.

Acoustic–structure interaction simulation

The acoustic–structure module, using finite element (F.E.) solver COMSOL Multiphysics 5.3, is implemented to study the acoustic potential landscape as the result of the soft/hard, air-embedded PDMS structure interacting with the chamber fluid upon excitation. Fig. 2b provides the 2-D model geometry consisting of a top fluid and bottom solid for which we simulated water and PDMS, respectively; the center of the solid is an empty space representing the air cavity. The bottom boundaries of the solid are excited using a prescribed displacement in the y-direction, simulating the mode of vibration of the PZT along its thickness. An arbitrary isotropic loss factor (0.2) is factored into the simulation to account for the structural damping of the solid as in the case of PDMS. The resulting total acoustic pressure in the fluid is calculated by the F.E. solver, which solves the acoustic–structure interaction at the interface between the fluid and solid, as well as the inviscid momentum conservation equation (Euler's equation) and mass conservation equation (continuity equation) in the fluid. The simulation assumes classical pressure acoustics with isentropic thermodynamic processes and assumes time-harmonic waves. For a harmonic acoustic field, $v_{\mathrm{in}} = \frac{1}{i\omega\rho_0}\nabla p_{\mathrm{in}}$, where ω is the angular frequency in rad s^{-1}. The simulation not only allows post-processing of the acoustic potential landscape generated (Fig. 2c and d and S1†) using eqn (1b), but also enables studies of the 1st order velocity of the chamber fluid (Fig. 2a) and surface profile of the solid (Fig. 2b and S2†) as a function of E' and membrane size, respectively.

Acoustic pressure simulation

The acoustic pressure module, using finite element (F.E.) solver COMSOL Multiphysics 5.3, is implemented to simulate the pressure profile inside the device chamber. While the 3-D model geometry in Fig. 5c mimics the 2-D model in Fig. 2a, the bottom solid is treated as fluid rather than solid mechanics. This substitution eliminates the physics complication, as well as extra computing power, involved in the acoustic–structure interaction by considering only the materials' impedance (given by the speed of sound and density) to simulate the wave propagation. For the soft PDMS structure, arbitrary values of the speed of sound and density are used. Normal displacement in the direction of the y-axis is specified on the bottom of the solid, simulating the direction of PZT excitation. Plane wave radiation is assumed all around the boundaries of the top fluid, enabling the outgoing plane wave to leave the modeling domain with minimal reflections.

Thickness measurement of the PDMS membrane

The fabricated PDMS structures are cut to reveal the cross section of membranes, and 3 membranes are examined using

SEM. The measured thicknesses are 1.09 μm, 1.14 μm, and 1.33 μm, and their average thickness is approximately 2.18 μm. For simplicity, we assume a 2 μm membrane thickness to be used in our simulations.

Polystyrene beads

Both 1 μm and 10 μm fluorescent green polystyrene beads are obtained from Thermo Fisher Scientific, USA.

HeLa cell culturing

HeLa cells (American Type Culture Collection, ATCC) were maintained in Dulbecco's modified essential medium (DMEM, Corning) supplemented with 10% (vol/vol) fetal bovine serum (FBS, Thermo Scientific), 1% penicillin/streptomycin (Mediatech), and 1% sodium pyruvate (Corning). HeLa cells were kept in an incubator at 37 °C and 5% CO_2.

Author contributions

K.-W. T. is the main contributor who designed and fabricated the CMAP device, built the experimental setup, conducted the experiments, analyzed the data, and wrote the majority of the manuscript. K.-W. T. and P.-Y. C. shared the ideas for the project. P.-Y. C., Y.-F. C., and F.-L., Y. advised on the design of the experiments, the data analysis, and the manuscript. P.-S. C. and S. T. provided support to the numerical simulations. C. W. and T. M. prepared the HeLa cells for the experiments, as well as shared their knowledge in cell culturing.

Conflicts of interest

There are no conflicts to declare.

Acknowledgements

This work is supported by NSF ECCS 1711507. The LDV equipment was contributed by Polytech, Inc.; special thanks are given to Kasra Kakavand and Eric Lawrence for their assistance in performing the data measurements.

References

1 J. Nilsson, M. Evander, B. Hammarström and T. Laurell, *Anal. Chim. Acta*, 2009, **649**, 141–157.
2 J. Sun, N. Jamilpour, F.-Y. Wang and P. K. Wong, *Biomaterials*, 2014, **35**, 3273–3280.
3 D. K. Wood, D. M. Weingeist, S. N. Bhatia and B. P. Engelward, *Proc. Natl. Acad. Sci. U. S. A.*, 2010, **107**, 10008–10013.
4 D. J. Collins, A. Neild, A. deMello, A.-Q. Liu and Y. Ai, *Lab Chip*, 2015, **15**, 3439–3459.
5 L. Kang, *Drug Discovery Today*, 2008, **13**, 1–13.
6 L. Gervais, N. de Rooij and E. Delamarche, *Adv. Mater.*, 2011, **23**, H151–H176.
7 D. Taller, K. Richards, Z. Slouka, S. Senapati, R. Hill, D. B. Go and H.-C. Chang, *Lab Chip*, 2015, **15**, 1656–1666.
8 Y. Xiao, Y. Lu, M. Hsieh, J. Liao and P. K. Wong, *PLoS One*, 2016, **11**, e0154640.
9 C. M. Puleo, H.-C. Yeh and T.-H. Wang, *Tissue Eng.*, 2007, **13**, 2839–2854.
10 N. Jamilpour, K.-H. Nam, C. C. Gregorio and P. K. Wong, *ACS Biomater. Sci. Eng.*, 2019, **5**, 3808–3816.
11 W. Hu, Q. Fan and A. T. Ohta, *Lab Chip*, 2013, **13**, 2285–2291.
12 M.-C. Zhong, X.-B. Wei, J.-H. Zhou, Z.-Q. Wang and Y.-M. Li, *Nat. Commun.*, 2013, **4**, 1768.
13 A. Ashkin, J. M. Dziedzic and T. Yamane, *Nature*, 1987, **330**, 769–771.
14 H. Zhang and K.-K. Liu, *J. R. Soc., Interface*, 2008, **5**, 671–690.
15 B. Lim, V. Reddy, X. Hu, K. Kim, M. Jadhav, R. Abedini-Nassab, Y.-W. Noh, Y. T. Lim, B. B. Yellen and C. Kim, *Nat. Commun.*, 2014, **5**, 3846.
16 C.-T. Ho, R.-Z. Lin, R.-J. Chen, C.-K. Chin, S.-E. Gong, H.-Y. Chang, H.-L. Peng, L. Hsu, T.-R. Yew, S.-F. Chang and C.-H. Liu, *Lab Chip*, 2013, **13**, 3578–3587.
17 M.-Y. Chiang, Y.-W. Hsu, H.-Y. Hsieh, S.-Y. Chen and S.-K. Fan, *Sci. Adv.*, 2016, **2**, e1600964.
18 I.-F. Cheng, H.-C. Chang, D. Hou and H.-C. Chang, *Biomicrofluidics*, 2007, **1**, 021503.
19 H. N. Chia and B. M. Wu, *J. Biol. Eng.*, 2015, **9**, 4.
20 A. Panwar and L. P. Tan, *Molecules*, 2016, **21**, 685.
21 H. Bruus, *Lab Chip*, 2012, **12**, 1014–1021.
22 B. Raeymaekers, C. Pantea and D. N. Sinha, *J. Appl. Phys.*, 2011, **109**, 014317.
23 I. Leibacher, P. Reichert and J. Dual, *Lab Chip*, 2015, **15**, 2896–2905.
24 B. Hammarström, T. Laurell and J. Nilsson, *Lab Chip*, 2012, **12**, 4296–4304.
25 A. Castro and M. Hoyos, *Ultrasonics*, 2016, **66**, 166–171.
26 D. J. Collins, B. Morahan, J. Garcia-Bustos, C. Doerig, M. Plebanski and A. Neild, *Nat. Commun.*, 2015, **6**, 8686.
27 X. Ding, S.-C. S. Lin, B. Kiraly, H. Yue, S. Li, I.-K. Chiang, J. Shi, S. J. Benkovic and T. J. Huang, *Proc. Natl. Acad. Sci. U. S. A.*, 2012, **109**, 11105–11109.
28 F. Guo, Z. Mao, Y. Chen, Z. Xie, J. P. Lata, P. Li, L. Ren, J. Liu, J. Yang, M. Dao, S. Suresh and T. J. Huang, *Proc. Natl. Acad. Sci. U. S. A.*, 2016, **113**, 1522–1527.
29 A. K. Tay, M. Dhar, I. Pushkarsky and D. D. Carlo, *Lab Chip*, 2015, **15**, 2533–2537.
30 G. Destgeer and H. Jin Sung, *Lab Chip*, 2015, **15**, 2722–2738.
31 S.-C. Steven Lin, X. Mao and T. Jun Huang, *Lab Chip*, 2012, **12**, 2766–2770.
32 L. Y. Yeo and J. R. Friend, *Biomicrofluidics*, 2009, **3**, 012002.
33 Y. Chen, X. Ding, S.-C. S. Lin, S. Yang, P.-H. Huang, N. Nama, Y. Zhao, A. A. Nawaz, F. Guo, W. Wang, Y. Gu, T. E. Mallouk and T. J. Huang, *ACS Nano*, 2013, **7**, 3306–3314.
34 X. Ding, J. Shi, S.-C. Steven Lin, S. Yazdi, B. Kiraly and T. Jun Huang, *Lab Chip*, 2012, **12**, 2491–2497.

35 Y. Bian, F. Guo, S. Yang, Z. Mao, H. Bachman, S.-Y. Tang, L. Ren, B. Zhang, J. Gong, X. Guo and T. J. Huang, *Microfluid. Nanofluid.*, 2017, **21**, 132.
36 A. R. Rezk, J. K. Tan and L. Y. Yeo, *Adv. Mater.*, 2016, **28**, 1970–1975.
37 B. Kang, J. Shin, H.-J. Park, C. Rhyou, D. Kang, S.-J. Lee, Y. Yoon, S.-W. Cho and H. Lee, *Nat. Commun.*, 2018, **9**, 5402.
38 W. Connacher, N. Zhang, A. Huang, J. Mei, S. Zhang, T. Gopesh and J. Friend, *Lab Chip*, 2018, **18**, 1952–1996.
39 M. Alvarez, J. R. Friend and L. Y. Yeo, *Langmuir*, 2008, **24**, 10629–10632.
40 A. Marzo and B. W. Drinkwater, *Proc. Natl. Acad. Sci. U. S. A.*, 2019, **116**, 84–89.
41 K. Melde, A. G. Mark, T. Qiu and P. Fischer, *Nature*, 2016, **537**, 518–522.
42 I. Leibacher, S. Schatzer and J. Dual, *Lab Chip*, 2014, **14**, 463–470.
43 J.-H. Lee, K.-J. Lee, H.-G. Park and J.-H. Kim, *Ocean Eng.*, 2015, **103**, 160–170.
44 R. A. Freitas, *Nanomedicine*, Landes Bioscience, Austin, TX, 1999.
45 W. M. Haynes, *CRC Handbook of Chemistry and Physics*, CRC Press, Boca Raton, Fla., 92nd edn, 2011.
46 P. B. Muller, R. Barnkob, M. J. H. Jensen and H. Bruus, *Lab Chip*, 2012, **12**, 4617.
47 A. Kovalenko, M. Fauquignon, T. Brunet and O. Mondain-Monval, *Soft Matter*, 2017, **13**, 4526–4532.
48 R. N. Palchesko, L. Zhang, Y. Sun and A. W. Feinberg, *PLoS One*, 2012, **7**, e51499.
49 W. S. Hanoosh and E. M. Abdelrazaq, *Malaysian Polymer*, 2009, **4**, 52–61.
50 W. Xu, N. Chahine and T. Sulchek, *Langmuir*, 2011, **27**, 8470–8477.
51 M. Dorrestijn, A. Bietsch, T. Açıkalın, A. Raman, M. Hegner, E. Meyer and C. Gerber, *Phys. Rev. Lett.*, 2007, **98**, 026102.
52 K. Latifi, H. Wijaya and Q. Zhou, *Phys. Rev. Lett.*, 2019, **122**, 184301.
53 M. K. Tan, J. R. Friend and L. Y. Yeo, *Appl. Phys. Lett.*, 2007, **91**, 224101.
54 D. Hartono, Y. Liu, P. Lin Tan, X. Y. Sherlene Then, L.-Y. Lanry Yung and K.-M. Lim, *Lab Chip*, 2011, **11**, 4072–4080.
55 M. Evander, L. Johansson, T. Lilliehorn, J. Piskur, M. Lindvall, S. Johansson, M. Almqvist, T. Laurell and J. Nilsson, *Anal. Chem.*, 2007, **79**, 2984–2991.
56 D. Bazou, W. T. Coakley, A. J. Hayes and S. K. Jackson, *Toxicol. In Vitro*, 2008, **22**, 1321–1331.
57 I. Leibacher, P. Hahn and J. Dual, *Microfluid. Nanofluid.*, 2015, **19**, 923–933.
58 F.-M. Boisvert, Y. Ahmad, M. Gierliński, F. Charrière, D. Lamond, M. Scott, G. Barton and A. I. Lamond, *Mol. Cell. Proteomics*, 2011, **11**, M111.011429.
59 H. Bruus, *Lab Chip*, 2011, **12**, 20–28.
60 J. K. Tsou, J. Liu, A. I. Barakat and M. F. Insana, *Ultrasound Med. Biol.*, 2008, **34**, 963–972.
61 N. Nama, R. Barnkob, Z. Mao, C. J. Kähler, F. Costanzo and T. Jun Huang, *Lab Chip*, 2015, **15**, 2700–2709.
62 E. Verneuil, A. Buguin and P. Silberzan, *EPL*, 2004, **68**, 412.
63 G. C. Randall and P. S. Doyle, *Proc. Natl. Acad. Sci. U. S. A.*, 2005, **102**, 10813–10818.
64 J. Friend and L. Yeo, *Biomicrofluidics*, 2010, **4**, 026502.

